Highlights

Oscillatory Stability and Harmonics Analysis of Electro-mechanical Coupling in PMSG-WTs via Impedance Modeling

Bin Liu,Ruiting Sun,Zhen Li,Long Sheng,Samson S. Yu

- A detailed impedance model for PMSG-WTs considering electro-mechanical coupling is proposed.
- The effect of electro-mechanical coupling on the output impedance characteristic is analyzed.
- An explicit description of harmonic transfer relationship between mechanical and electrical subsystems is introduced.

Oscillatory Stability and Harmonics Analysis of Electro-mechanical Coupling in PMSG-WTs via Impedance Modeling⋆

Bin Liu[a], Ruiting Sun [a], Zhen Li [b,*], Long Sheng[a] and Samson S. Yu[c]

[a]College of Artificial Intelligence, China University of Petroleum (Beijing), Beijing 102249, China
[b]School of Automation and Key Laboratory for Intelligent Control & Decision on Complex Systems, Beijing Institute of Technology, Beijing 100081, China
[c]School of Engineering, Faculty of Science, Engineering and Built Environment, Burwood, Melbourne, 3125, Australia.

ARTICLE INFO

Keywords:
Electrical oscillations
Impedance modeling
Electro-mechanical coupling
Permanent magnet synchronous generator

ABSTRACT

The output dynamic characteristics of permanent magnet synchronous generator (PMSG) wind turbines (WTs) significantly influence system damping and, consequently, the stability of system electrical oscillations. It is generally assumed that these characteristics are determined solely by the electrical subsystem due to the relatively soft shaft. However, with the sharply increasing capacity, the PMSG's shaft inevitably becomes stronger, yet there are few studies verifying its significance in the coupling between mechanical and electrical subsystems when investigating electrical oscillations in grid-connected PMSG-WTs systems. In this paper, an impedance model of PMSG-WTs, including both the mechanical shaft subsystem and the electrical subsystem, is established to specifically examine electrical oscillation issues. Based on this impedance model, the mechanism of electro-mechanical coupling on harmonic transfer within the PMSG-WTs is studied, revealing the non-negligible influence of the mechanical subsystem on the output impedance characteristic of PMSG-WTs. It is demonstrated that the mechanical shaft subsystem, with different rotor inertia and shaft damping coefficients, affects the harmonic transfer between mechanical and electrical subsystems, thereby impacting the output impedance characteristics of PMSG-WTs and system electrical oscillation stability. Finally, simulation results verify the effect of electro-mechanical coupling on system stability.

1. Introduction

With advantages such as low cost, high efficiency, and high output power, permanent magnet synchronous generator (PMSG) wind turbines (WTs) have become widely adopted in large-scale wind power generation systems [1, 2, 3]. However, the increasing penetration of renewable energy and the widespread use of power electronic devices have resulted in weaker system damping and potential vulnerabilities to unstable operation. Oscillation incidents in large-scale grid-connected wind farm systems have become significant concerns for the safety of power systems [4, 5]. In July 2015, wind farms in Hami, China, which primarily used PMSG-WTs, experienced severe oscillation accidents. These incidents led to the tripping of numerous wind turbine generators and caused shaft torsional vibrations in three nearby thermal power generators [6, 7, 8].

The oscillation issues in grid-connected wind farms can be categorized into drive-train torsional oscillations and electrical oscillations. Wind turbines are connected to the PMSG rotor through the mechanical shaft, and unbalanced torque generates varying relative angular displacements among each shaft segment. This may lead to drive-train torsional oscillations and early fatigue of mechanical components [9, 10]. Additionally, electrical oscillations manifest as periodic fluctuations in electrical quantities such as voltage, current, and power, resulting in significant harmonics across a wide frequency range and even power divergence [11].

Numerous studies have examined drive-train torsional oscillations in power systems using small-signal modeling analysis methods. In [12], the mechanism of drivetrain oscillation in grid-forming PMSG-WTs was analyzed using a linearized model in the frequency domain, revealing that damping control in the machine-side converter (MSC) can suppress drivetrain oscillations. Researchers in [13] described the motion of wind turbines coupled to generators using a five-degree-of-freedom model and developed a control law based on sliding mode theory to mitigate torsional vibrations in doubly-fed induction generator (DFIG)-WTs. The shaft torsional vibration analysis of synchronous generators was conducted in [14, 15] using a linearized small-signal model of the entire system, including both mechanical shaft and electrical subsystems. It was found that current and voltage harmonics in the electrical subsystem contribute to fluctuations in electromagnetic torque, leading to perturbations in shaft rotating angles and severe shaft torsional vibrations.

On the other hand, small-signal modeling and associated analysis methods have been employed to study electrical oscillations in PMSG-based wind farms integrated into the grid, mainly using state-space methods [16] and impedance-based methods [17]. If the impedance between WTs and the grid constitutes an RLC series resonant circuit with negative resistance or insufficient stability margin, the circuit risks

⋆This work was supported in part by the National Natural Science Foundation of China under Grant 52225702, in part by the Science Foundation of China University of Petroleum, Beijing (No.2462024YJRC007), and in part by the Australian Research Council IC210100021.

*Corresponding author
liubin6410@126.com (B. Liu); sunruiting0306@163.com (Ruiting Sun); zhenli@bit.edu.cn (Zhen Li); shenglong@cup.edu.cn (Long Sheng); samson.yu@deakin.edu.au (S.S. Yu)
ORCID(s): 0000-0003-3031-9592 (B. Liu)

electrical oscillation even under small disturbances [18]. Initially, grid-connected PMSG-based wind farms were simplified into voltage-source converter (VSC) models for electrical oscillation analysis [11, 19]. In [20], a state-space model of the VSC was built to represent PMSG-WTs, including DC-link, converter vector control, phase-locked loop (PLL), and grid dynamics. This model demonstrated low-frequency and sub-synchronous frequency oscillations by obtaining eigenvalue loci. It was found that DC-link dynamics, MSC, and the generator significantly influence the overall WT's output characteristics and affect modeling accuracy and system stability analysis [21, 22, 23]. The influence of DC-link behaviors on system characteristics and stability was deeply studied in [21], with a detailed impedance model of PMSG-WTs considering MSC, DC-link, and the generator, concluding that weakly damped DC-link dynamics can destabilize grid-connected systems. Authors in [22] investigated the shaping effect of controllers in MSC and grid-side converter (GSC) on PMSG external impedance characteristics, indicating that MSC control parameters significantly impact the system stability margin.

Currently, it is generally considered that the dynamic characteristics of grid-connected WT systems are dominated by the electrical subsystem. The interaction between the mechanical shaft subsystem and the electrical subsystem, known as the electro-mechanical coupling effect, is often neglected in the analysis of electrical oscillations. With substantially increased output capacity, leading to a much stronger rotor-connected shaft, it is natural to question whether the mechanical shaft subsystem should be excluded from PMSG-WTs' small-signal modeling for electrical oscillation analysis. Existing research provides few insights into the effectiveness of neglecting the mechanical subsystem and electro-mechanical coupling effect when investigating electrical oscillation issues. Thus, it becomes necessary to verify the impact of the electro-mechanical coupling effect on the dynamic characteristics of grid-connected PMSG-WTs, which determine electrical oscillation risks. This is one of the main motivations of this paper.

Towards this focus, only a handful of studies specifically address the impact of the electro-mechanical coupling effect on the electrical oscillations of grid-connected WT systems. In [24], the drive-train dynamics were modeled using both one-mass and two-mass mechanical models to establish the output impedance of grid-connected PMSG-WTs. It was found that rotational angle disturbances in the mechanical shaft subsystem affect the output current and voltage, significantly influencing electrical oscillation stability. Authors in [25] studied torsional vibrations in type-IV WTs interfaced to the grid through grid-forming GSCs, finding that grid frequency variations result in reactions of generator electromagnetic torque, which may propagate to the power grid. However, explicit knowledge of the coupling paths between the electrical and mechanical subsystems was not provided in [24, 25], which is necessary to deeply understand the electro-mechanical coupling effect mechanism. Revealing this complex mechanism is another motivation of this paper.

Therefore, this paper investigates the small-signal output impedance model of PMSG-WTs in the *abc*-frame, considering both the mechanical shaft subsystem and the electrical subsystem with their associated coupling. The mechanical drive-train dynamics are described by a two-mass-spring model. Based on this modeling, the effect of electro-mechanical coupling on the output impedance characteristic is studied to determine the impact of the mechanical subsystem on electrical oscillation stability. By establishing the explicit harmonic transfer relationship between the mechanical and electrical subsystems, the interaction mechanism between these subsystems is clearly explained.

The rest of the paper proceeds as follows: Section 2 proposes the sequence impedance model of grid-connected PMSG-WTs, including mechanical and electrical subsystems, and verifies the impedance model through frequency-sweeping measurement results in MATLAB/Simulink. Section 3 studies the influence of the electro-mechanical coupling effect on impedance characteristics, revealing the interaction between mechanical and electrical subsystems. Section 4 conducts stability analysis for a case study and oscillation simulation to verify the effect of electro-mechanical coupling on system stability. Section 5 concludes the paper.

2. Impedance Model of Grid-Connected PMSG-WTs

Overall, the PMSG-WT system consists of a mechanical subsystem and an electrical subsystem. The mechanical subsystem is mainly composed of a wind turbine connected to the synchronous generator through the coupling shaft, while the electrical subsystem includes the MSC, GSC, and DC-link. The conventional structure and control block diagram of the PMSG-WT system is shown in Fig. 1. v_{abc} and i_{gabc} represent the three-phase voltage and current at the point of common connection (PCC), and v_{iabc} is the output voltage of GSC. v_{sabc} and i_{sabc} represent the voltage and current at MSC output. m_{iabc} and m_{sabc} are the GSC and MSC output modulation signals. $V^{\mathrm{ref}}\mathrm{dc}$ denotes the DC-bus voltage reference, and $C\mathrm{dc}$ is the DC-bus capacitor. L_{f} and C_{f} are the inductance and capacitance of the filter, respectively. The grid voltage angle at PCC, θ_{PLL}, is captured by PLL. The rotor electrical speed and angular position are represented as ω_{r} and θ_{r}.

Based on the harmonic linearization method [26], a positive voltage harmonic is analytically superimposed from PCC at frequency f_{p} on the steady-state point at the fundamental frequency f_1. The positive voltage harmonic is represented as $\hat{V}\mathrm{p} = V\mathrm{p}e^{j\phi\mathrm{vp}}$, where $V\mathrm{p}$ and ϕ_{vp} are the magnitude and the phase. Due to the non-linearity of PLL and asymmetry of the dq current regulators, when the positive-sequence voltage harmonic $\hat{V}\mathrm{p}$ is injected, the output current response consists of the positive-sequence harmonic $\hat{I}\mathrm{gp}$ at f_{p} and negative-sequence $\hat{I}\mathrm{gn}$ at $f' = f\mathrm{p} - 2f_1$, whose phenomenon is defined as the frequency

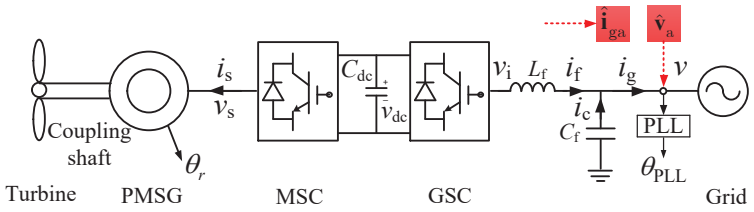

Fig. 1. Main structure of grid-connected PMSG-WTs system

coupling [27]. The harmonic components can be represented in matrix form, which helps describe the distribution and transfer relationship between harmonics. The harmonic matrices of PCC voltage, GSC output voltage, and current are shown as:

$$\hat{\mathbf{v}}_{\mathrm{a}} = \begin{bmatrix} \hat{V}_{\mathrm{p}}(f_{\mathrm{p}}) \\ \hat{V}_{\mathrm{n}}(f') \end{bmatrix}, \hat{\mathbf{v}}_{\mathrm{ia}} = \begin{bmatrix} \hat{V}_{\mathrm{ip}}(f_{\mathrm{p}}) \\ \hat{V}_{\mathrm{in}}(f') \end{bmatrix}, \hat{\mathbf{i}}_{\mathrm{ga}} = \begin{bmatrix} \hat{I}_{\mathrm{gp}}(f_{\mathrm{p}}) \\ \hat{I}_{\mathrm{gn}}(f') \end{bmatrix}. \quad (1)$$

The power harmonic can be transferred to the DC-link due to the power balance between the AC-port and the DC-port of GSC, which results into the DC-link voltage harmonic $\hat{V}_{\mathrm{dc}}(f_{\mathrm{p}} - f_1)$.

Due to the rotor flux oriented control strategy and the DC-link voltage harmonic $\hat{V}_{\mathrm{dc}}$, the output voltage and current of MSC will contain harmonics at frequencies $f_{\mathrm{p}} - f_1 + f_{\mathrm{r}}$ and $f_{\mathrm{p}} - f_1 - f_{\mathrm{r}}$, as follows,

$$\hat{\mathbf{v}}_{\mathrm{sa}} = \begin{bmatrix} \hat{V}_{\mathrm{sp}}(f_{\mathrm{p}} - f_1 + f_{\mathrm{r}}) \\ \hat{V}_{\mathrm{sn}}(f_{\mathrm{p}} - f_1 - f_{\mathrm{r}}) \end{bmatrix}, \hat{\mathbf{i}}_{\mathrm{sa}} = \begin{bmatrix} \hat{I}_{\mathrm{sp}}(f_{\mathrm{p}} - f_1 + f_{\mathrm{r}}) \\ \hat{I}_{\mathrm{sn}}(f_{\mathrm{p}} - f_1 - f_{\mathrm{r}}) \end{bmatrix}. \quad (2)$$

Therefore, the relationship between the voltage and current harmonics at PCC can be modeled as follows.

$$\mathbf{Y}_{\mathrm{PMSG}} \cdot \hat{\mathbf{v}}_{\mathrm{a}} = -\hat{\mathbf{i}}_{\mathrm{ga}}, \quad (3)$$

where the admittance components can be rewritten in the matrix form as

$$\mathbf{Y}_{\mathrm{PMSG}} = \begin{bmatrix} Y^{\mathrm{p}}_{\mathrm{PMSG}}(s) & Y^{\mathrm{r}}_{\mathrm{PMSG}}(s) \\ Y^{\mathrm{c}}_{\mathrm{PMSG}}(s) & Y^{\mathrm{n}}_{\mathrm{PMSG}}(s') \end{bmatrix}. \quad (4)$$

where $s' = 2\pi f'$.

When only the electrical subsystem is considered, the mechanical rotor angle remains fixed at steady state during the modeling of the overall sequence impedance. However, the introduction of the mechanical drive-train dynamics will lead to perturbations in the rotor angle, which will be described in the following section.

2.1. Drive Train Dynamics

The mechanical structure of the turbine-generator shaft system is shown in Fig. 2(a), including the impeller vane, the rotor of the generator, and the bearing between the impeller vane and the rotor. The primary mechanical torque generated by the wind-driven impeller vane acts on the bearing, causing it to rotate. This, in turn, exerts an electromagnetic torque on the generator rotor due to the interaction between the generator's magnetic field and winding current. The combined

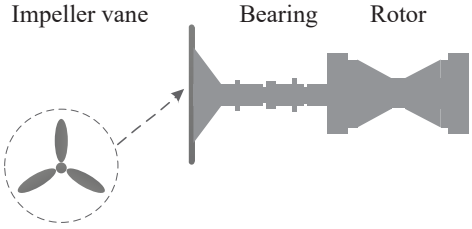

(a) Mechanical structure of the turbine-generator shaft system

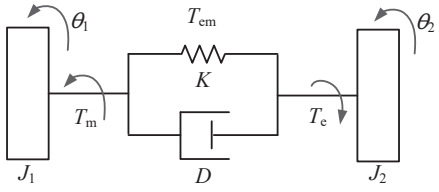

(b) Two mass-spring mechanical subsystem model

Fig. 2. The drive-train structure in PMSG-WTs system

effect of this electromagnetic torque and the mechanical torque transmitted by the bearing turns the generator rotor to produce electrical current.

In general, the bearing can be simplified as a torsional spring to retain its spring characteristics, and both the impeller vane and the rotor can be considered as two smooth rigid bodies. Consequently, the mechanical subsystem under study is represented by a two-mass spring model [24]. In this model, each mass is treated as an equivalent rigid concentrated mass block, and the masses are connected by a massless spring. The two-mass spring mechanical model is illustrated in Fig. 2(b), where J_1 and J_2 denote the inertia of the wind turbine and the PMSG rotor, respectively. K and D represent the stiffness and damping coefficient of the coupling shaft, while T_{m}, T_{e}, and T_{em} denote the mechanical torque, electromagnetic torque, and coupling shaft torque, respectively. Therefore, the drive-train dynamics of the mechanical subsystem can be described as follows:

$$\begin{aligned} J_1 \frac{d\omega_1}{dt} &= T_{\mathrm{m}} - T_{\mathrm{em}}, \\ J_2 \frac{d\omega_2}{dt} &= T_{\mathrm{em}} - T_{\mathrm{e}}, \\ T_{\mathrm{em}} &= D(\omega_1 - \omega_2) + K(\theta_1 - \theta_2). \end{aligned} \quad (5)$$

Here, θ_1 and ω_1 are the mechanical angular position and speed of turbine. θ_2 and ω_2 are the mechanical angular position and speed of PMSG rotor. Their relationship can be expressed as

$$\omega_1 = \frac{d\theta_1}{dt}, \omega_2 = \frac{d\theta_2}{dt}. \tag{6}$$

During operation, the mechanical torque, electromagnetic torque, and coupling shaft torque collectively act on the shaft, causing a relative angular displacement between the two mass blocks, which remains fixed when the system is stable. When a small-signal perturbation occurs at the PCC voltage, it induces a small disturbance in the electromagnetic torque T_e, leading to an imbalance between the mechanical torque and electromagnetic torque applied to the shaft. This imbalance results in small disturbances in the angular positions of the two mass blocks, $\hat{\theta}_1$ and $\hat{\theta}_2$, causing torsional vibrations of the shaft due to the varying relative angular displacement between the mass blocks. The corresponding small-signal perturbation model can be calculated as:

$$\begin{aligned} \hat{\theta}_1 &= M_1(s)\hat{\theta}_2, \\ \hat{T}_e &= M(s)\hat{\theta}_2, \end{aligned} \tag{7}$$

where the transfer function of the drive-train dynamic of coupling shaft is

$$\begin{aligned} M_1(s) &= \frac{Ds + K}{J_1 s^2 + Ds + K}, \\ M(s) &= (J_2 s^2 + Ds + K) - \frac{(Ds + K)^2}{J_1 s^2 + Ds + K}. \end{aligned} \tag{8}$$

In addition, the electrical angular position disturbance $\hat{\theta}_r = p \cdot \hat{\theta}_2$, where p is the number of pole-pairs.

2.2. Impedance Modeling of Generator

In the three-phase stationary coordinate frame, the stator voltage equation and the flux linkage equation of the PMSG are represented as

$$\begin{aligned} v_{sa} &= R_s i_{sa} + \frac{d\psi_a}{dt}, \\ v_{sb} &= R_s i_{sb} + \frac{d\psi_b}{dt}, \\ v_{sc} &= R_s i_{sc} + \frac{d\psi_c}{dt}, \end{aligned} \tag{9}$$

$$\begin{bmatrix} \psi_a \\ \psi_b \\ \psi_c \end{bmatrix} = \begin{bmatrix} L_{aa} & L_{ab} & L_{ac} \\ L_{ba} & L_{bb} & L_{bc} \\ L_{ca} & L_{cb} & L_{cc} \end{bmatrix} \begin{bmatrix} i_{sa} \\ i_{sb} \\ i_{sc} \end{bmatrix} + \begin{bmatrix} \psi_{am} \\ \psi_{bm} \\ \psi_{cm} \end{bmatrix}, \tag{10}$$

where R_s is the resistance of each phase winding of the stator. ψ_a, ψ_b, $\psi_c$are the three-phase stator flux linkage. ψ_{am}, ψ_{bm}, ψ_{cm} are the projection of the permanent magnet flux linkage on each phase winding. L_{aa}, L_{bb}, L_{cc} are the self-inductance of each phase stator winding. L_{ab}, L_{ac}, L_{ba}, L_{bc}, L_{ca}, L_{cb} are the mutual inductance among various phases.

The current in the stator winding interacts with the flux field to generate the electromagnetic force, which, in turn, produces the electromagnetic torque. This torque acts in opposition to the mechanical torque, thereby resisting the rotation of the rotor. The electromagnetic torque can be expressed in the time domain as

$$T_e = 1.5p[\psi_m i_{qs} + (L_d - L_q) i_{ds} i_{qs}], \tag{11}$$

where L_d and L_q are the stator inductance along the dq-axis, respectively.

Applying the symmetrical component method to the voltage and flux linkage equations of the synchronous generator, the relationship among voltage harmonics, current harmonics, and rotor angular position disturbance can be linearized as follows,

$$\mathbf{G_1}\hat{\mathbf{v}}_{sa} = \mathbf{G_2}\hat{\mathbf{i}}_{sa} + \mathbf{G_3}\hat{\theta}_r. \tag{12}$$

Due to the electromagnetic torque disturbance caused by stator current harmonics, this disturbance acts on the rotor mass block, generating the electrical angular position disturbance $\hat{\theta}_r$. According to the Parker and inverse Parker transformations as discussed in [26], the relationship between the rotor mechanical angular position perturbation $\hat{\theta}_r$ and stator current harmonics can be established by combining the small-signal disturbance of electromagnetic torque in (7) and (11). This relationship can be expressed as follows:

$$\hat{\theta}_r = \mathbf{T}\hat{\mathbf{i}}_{sa}. \tag{13}$$

The detailed coefficient matrices $\mathbf{G_1}$, $\mathbf{G_2}$, $\mathbf{G_3}$ and $\mathbf{T}$ are presented in the Appendix A.

2.3. Impedance Modeling of PMSG-WTs

The conventional control design for the back-to-back PWM converters, including the Machine-Side Converter

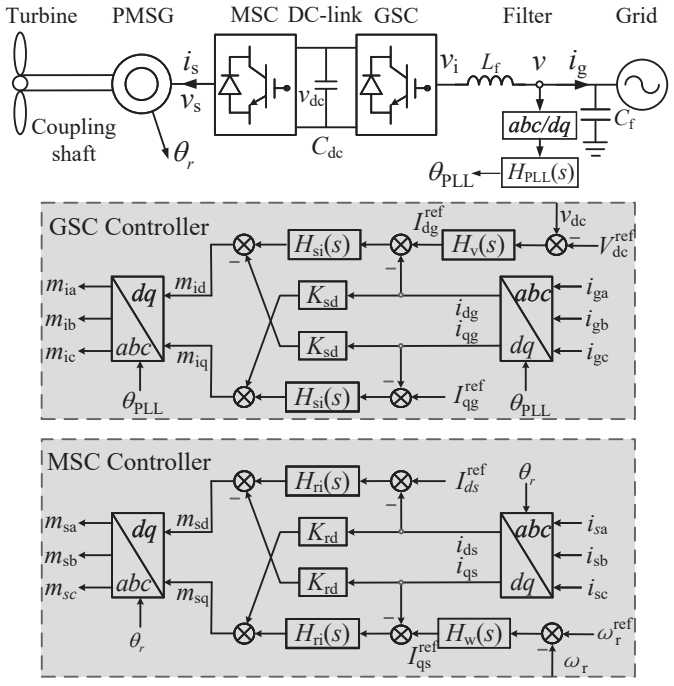

Fig. 3. The back-to-back PWM converters controller structure in PMSG-WTs system

(MSC) and Grid-Side Converter (GSC), is illustrated in Fig. 3. The MSC controller is designed to achieve Maximum Power Point Tracking (MPPT) by generating the corresponding modulation signals through the rotating speed loop and current loop. In contrast, the GSC controller is responsible for maintaining a constant DC bus voltage, ensuring a balanced power flow between the GSC and MSC. The transfer function of the PI controller for the Phase-Locked Loop (PLL) is denoted as $H_{\mathrm{PLL}}(s)$, and $T_{\mathrm{PLL}}(s)$ represents the closed-loop transfer function, which can be expressed as follows:

$$\begin{aligned} H_{\mathrm{PLL}}(s) &= (K_{\mathrm{pp}} + \frac{K_{\mathrm{pi}}}{s})\frac{1}{s}, \\ T_{\mathrm{PLL}}(s) &= \frac{H_{\mathrm{PLL}}(s)}{1 + V_1 H_{\mathrm{PLL}}(s)}. \end{aligned} \tag{14}$$

Besides, $H_{\mathrm{si}}(s)$ and $H_{\mathrm{v}}(s)$ represent the PI controller transfer functions of current loop and DC voltage loop in GSC. $H_{\mathrm{ri}}(s)$ and $H_{\mathrm{w}}(s)$ describe the transfer functions of current loop and rotating speed loop in MSC as follows.

$$\begin{aligned} H_{\mathrm{si}}(s) &= K_{\mathrm{ip}} + \frac{K_{\mathrm{ii}}}{s}, \\ H_{\mathrm{v}}(s) &= K_{\mathrm{vp}} + \frac{K_{\mathrm{vi}}}{s}, \\ H_{\mathrm{ri}}(s) &= K_{\mathrm{rp}} + \frac{K_{\mathrm{ri}}}{s}, \\ H_{\mathrm{w}}(s) &= K_{\mathrm{wp}}\frac{K_{\mathrm{wi}}}{s}. \end{aligned} \tag{15}$$

Moreover, the GSC output voltage equation, MSC output voltage equation, the circuitry model of the filter inductance, and the DC-bus voltage dynamic equation in the time domain can be described as follows:

$$\begin{aligned} L_{\mathrm{f}}\frac{di_{\mathrm{fa}}}{dt} &= v_{\mathrm{ia}} - v_{\mathrm{a}}, \\ C_{\mathrm{f}}\frac{dv_{\mathrm{a}}}{dt} &= i_{\mathrm{fa}} - i_{\mathrm{ga}}, \\ v_{\mathrm{ia}} &= K_{\mathrm{m}} v_{\mathrm{dc}} m_{\mathrm{ia}}, \\ v_{\mathrm{sa}} &= K_{\mathrm{m}} v_{\mathrm{dc}} m_{\mathrm{sa}}, \\ C_{\mathrm{dc}}\frac{\mathrm{d}v_{\mathrm{dc}}}{\mathrm{d}t} v_{\mathrm{dc}} &= \sum_{n=\mathrm{a,b,c}} (-v_{sn} i_{sn} - v_{in} i_n), \end{aligned} \tag{16}$$

where K_{m} is the modulation coefficient. The modulation m_{iabc} and m_{sabc} are the outputs from the double closed-loop controllers in the GSC and MSC, which both adopt the DC voltage harmonic $\hat{V}_{\mathrm{dc}}(f_{\mathrm{p}} - f_1)$.

According to the harmonic linearization method, the multiplication operator in the time domain is replaced by the convolution operator in the frequency domain. In this method, only the first-order harmonics are retained while higher-order harmonics are ignored. The relationship between harmonics at each port can thus be transformed into the frequency domain and expressed as:

Table 1
Parameters of PMSG-WT system.

	Parameter	Value
1	Rated power (S)	1.5 MVA
2	DC-link voltage (V_{dc})	1150 V
3	Rated voltage (V_1)	690 V
4	DC-link capacitor (C_{dc})	12.96 mF
5	Filter inductance (L_{f})	75 μH
6	Filter capacitor (C_{f})	600 μF
7	Rotor speed frequency (f_{r})	80 Hz
8	Inertia time constant (T_{J1})	8.56 s
9	Inertia time constant (T_{J2})	0.86 s
10	Stiffness coefficient (K)	1.2 p.u.
11	Damping coefficient (D)	1.5 p.u.

$$\begin{aligned} \mathbf{L}\hat{\mathbf{i}}_{\mathrm{fa}} &= \hat{\mathbf{v}}_{\mathrm{ia}} - \hat{\mathbf{v}}_{\mathrm{a}}, \\ \mathbf{C}\hat{\mathbf{v}}_{\mathrm{a}} &= \hat{\mathbf{i}}_{\mathrm{fa}} - \hat{\mathbf{i}}_{\mathrm{ga}}, \\ \hat{\mathbf{v}}_{\mathrm{ia}} &= \mathbf{P}_1\hat{V}_{\mathrm{dc}} + \mathbf{P}_2\hat{\mathbf{i}}_{\mathrm{ga}} + \mathbf{P}_3\hat{\mathbf{v}}_{\mathrm{a}}, \\ \hat{\mathbf{v}}_{\mathrm{sa}} &= \mathbf{Q_1}\hat{V}_{\mathrm{dc}} + \mathbf{Q_2}\hat{\mathbf{i}}_{\mathrm{sa}} + \mathbf{Q_3}\hat{\theta}_{\mathrm{r}}, \\ \hat{\mathbf{V}}_{dc} &= \mathbf{E}_1\hat{\mathbf{v}}_{ia} + \mathbf{E}_2\hat{\mathbf{i}}_{ga} + \mathbf{E}_3\hat{\mathbf{v}}_{sa} + \mathbf{E}_4\hat{\mathbf{i}}_{sa}, \end{aligned} \tag{17}$$

where the filter inductance and capacitor matrices are formulated as $\mathbf{L} = \mathrm{diag}[sL_{\mathrm{f}}, s'L_{\mathrm{f}}]$ and $\mathbf{C} = \mathrm{diag}[sC_{\mathrm{f}}, s'C_{\mathrm{f}}]$.

According to the relationship between the harmonics in (17), the admittance model of the PMSG-WT can be obtained as

$$\mathbf{Y}_{\mathrm{PMSG}}(s) = \mathbf{C} + \frac{\mathbf{E} - (\mathbf{P}_1\mathbf{E}_1 + \mathbf{P}_3) - \mathbf{\Gamma}\mathbf{Q}_1\mathbf{E}_1}{\mathbf{L} - (\mathbf{P}_1\mathbf{E}_1\mathbf{L} + \mathbf{P}_1\mathbf{E}_2 + \mathbf{P}_2) - \mathbf{\Gamma}(\mathbf{Q}_1\mathbf{E}_1\mathbf{L} + \mathbf{Q}_1\mathbf{E}_2)}, \tag{18}$$

where $\mathbf{E}$ represents the identity matrix. Besides, the coefficient matrix $\mathbf{\Gamma}$ is described as

$$\mathbf{\Gamma} = \frac{\mathbf{P}_1\mathbf{E}_3\mathbf{G}_1^{-1}(\mathbf{G}_2 + \mathbf{G}_3\mathbf{T}) + \mathbf{P}_1\mathbf{E}_4}{(\mathbf{E} - \mathbf{Q}_1\mathbf{E}_3)\mathbf{G}_1^{-1}(\mathbf{G}_2 + \mathbf{G}_3\mathbf{T}) - \mathbf{Q}_1\mathbf{E}_4 - \mathbf{Q}_2 - \mathbf{Q}_3\mathbf{T}}. \tag{19}$$

The detailed coefficient matrices are depicted in Appendix A.

2.4. Impedance Model Validation

Due to the frequency coupling effect, the impedance model of a PMSG-based wind farm exhibits multi-input and multi-output (MIMO) characteristics. To apply conventional Nyquist theory, the MIMO system must be transformed into a single-input and single-output (SISO) system using the impedance-based equivalent modeling approach, as described in references like [28] and [29]. The stability of this equivalent SISO system can be analyzed by applying the Nyquist criterion to the ratio of equivalent positive-sequence impedance, i.e., $Z^{\mathrm{p}}_{\mathrm{grid}}(s)/Z^{\mathrm{p}}_{\mathrm{equ}}(s)$, and the ratio of equivalent negative impedance, i.e., $Z^{\mathrm{n}}_{\mathrm{grid}}(s)/Z^{\mathrm{n}}_{\mathrm{equ}}(s)$. The resultant stability analysis using these ratios is shown to be consistent

with the stability analysis obtained using the general Nyquist criterion (GNC) for the MIMO system.

To validate the accuracy of the proposed analytical impedance model of the PMSG-WT, a simulation is carried out in MATLAB/Simulink. The simulation model includes a PMSG-WT connected to a weak grid with a short circuit ratio (SCR) of 2. The system parameters are listed in TABLE 1, which are obtained from a commercial PMSG-WT used in the wind farm in Hami, China. Since the inertia time constants T_{J1} and T_{J2} provide a more intuitive representation of the moments of inertia J_1 and J_2, using these time constants facilitates understanding and comparing the inertia characteristics. Therefore, in the subsequent sections, the time constants T_{J1} and T_{J2} will be used to represent the inertia.

The equivalent impedance of the wind turbine is measured using the perturbation injection method with frequency sweeping, as adopted from [30], and compared with the corresponding analytical results, as shown in Fig. 4. The analytical positive- and negative-sequence impedances are depicted with solid lines, which closely match the measured impedances represented by dotted lines across the entire frequency range. This validates the proposed model. To further compare the impedance characteristics with and without considering the mechanical shaft system and the electro-mechanical coupling effect, two scenarios are set up in the grid-connected PMSG-WT simulation model: one including the shaft system and one without (i.e., the PMSG input is set to a fixed rotating speed). Frequency sweeping tests are performed in both scenarios to obtain the impedance curves and compare the differences in impedance characteristics.

The comparison results are demonstrated in Fig. 5, illustrating the main differences in impedance characteristics between considering and not considering the shaft system model, particularly in the sub-synchronous and super-synchronous frequency ranges. As observed, the maximum difference in magnitude reaches nearly 10 dB, and the phase difference reaches 260 degrees in the super-synchronous frequency range of 65-100 Hz. Additionally, minor differences

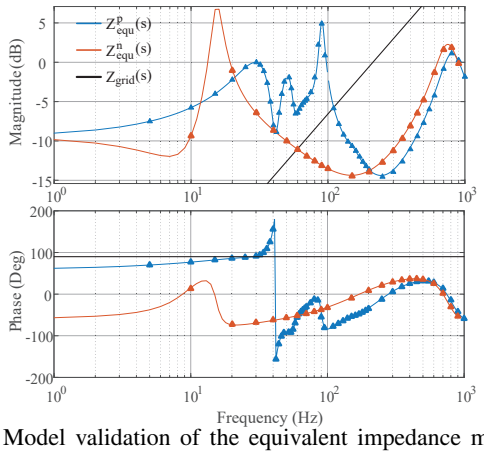

Fig. 4. Model validation of the equivalent impedance model of PMSG-WTs. Lines: analytical model. Dots: simulation measurement

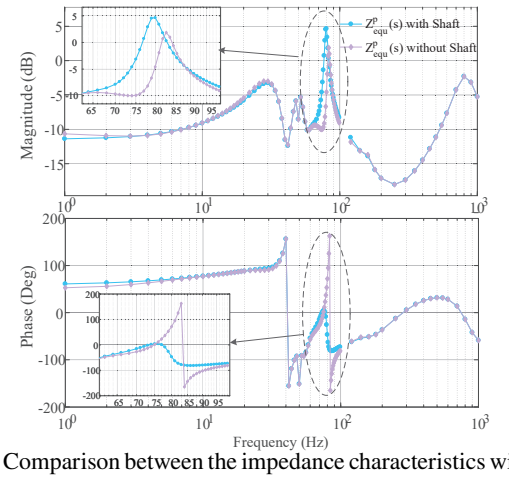

Fig. 5. Comparison between the impedance characteristics with and without the shaft system model

in magnitude and phase are noted in the sub-synchronous frequency range.

3. Electro-mechanical Coupling Effect Analysis

3.1. Harmonic Transfer Relationship

A block diagram of the small-signal model of PMSG-WTs is presented to describe the harmonics distribution and transfer relationship within the electrical subsystem in [22]. However, this model ignores the coupling effect between the electrical and mechanical subsystems, resulting in an incomplete analysis of harmonic transfer and not fully capturing the small-signal dynamics.

In this paper, the harmonics distribution and transfer relationship of PMSG-WTs is revisited, as shown in Fig. 6. This figure clearly demonstrates the conversion relationship between speed perturbations in the mechanical subsystem and harmonics in the electrical subsystem. The harmonic transfer relationship can be divided into two parts, which can be described as follows.

1) Electrical perturbations to mechanical perturbations

After injecting a small-signal voltage perturbation $\hat{V}_p$ at the PCC, voltage harmonics $\hat{\mathbf{v}}$sa and current harmonics $\hat{\mathbf{i}}$sa are generated at the stator of the PMSG. These harmonics are influenced by GSC and MSC modulation, as well as the power transfer between the AC and DC ports at the DC-bus. This transfer part is described in [22].

The stator current harmonic $\hat{\mathbf{i}}$sa causes perturbations in the electromagnetic torque $\hat{T}$e. This interaction with the constant primary mechanical torque results in disturbances in the rotor's angular speed $\hat{\omega}_r$ and, consequently, the electrical angular position disturbance $\hat{\theta}_r$. The red lines in Fig.6 and Fig.7 illustrate the transfer relationship between $\hat{\mathbf{i}}$sa and $\hat{\theta}$r, revealing the perturbation transfer routing from the electrical subsystem to the mechanical subsystem.

2) Mechanical perturbations to electrical perturbations

The rotor angular position disturbance $\hat{\theta}$r is integrated into the basic coordinate to achieve rotor flux-oriented control in the MSC controller. This process affects the stator

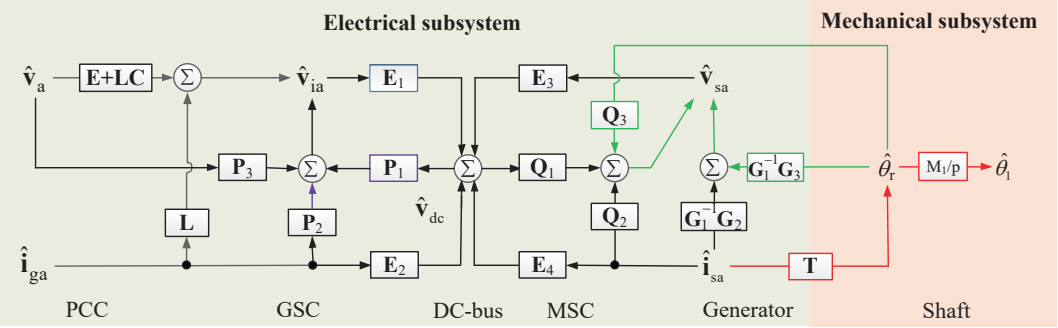

Fig. 6. Transfer relationship of harmonics in PMSG-WT

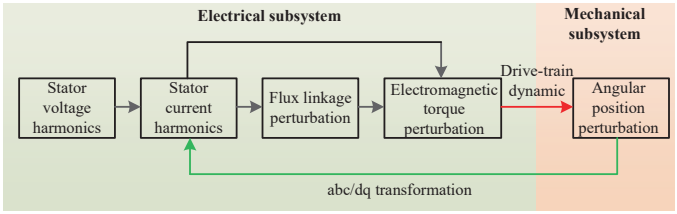

Fig. 7. Electro-mechanical coupling effect illustration in PMSG-WT

current harmonics in the dq-frame via the Park Transform. Consequently, the stator voltage harmonic $\hat{\mathbf{v}}$sa, which is modulated by the speed loop and current loop, will also change due to the perturbation on orientation. As a result, the stator voltage and current harmonics will be further transferred to the PCC through the back-to-back PWM converters and DC-bus, impacting the output current harmonics of PMSG-WTs. This process, which shows how perturbations in the mechanical subsystem affect electrical harmonics, is represented by the green lines in Fig.6 and Fig.7.

In summary, the output impedance characteristics of PMSG-WTs can be significantly influenced by the electro-mechanical coupling effect. This complex interaction between the electrical and mechanical subsystems involves a bidirectional process, where harmonics are transferred between the two subsystems. This coupling can lead to variations in the stability of electrical oscillations.

3.2. Influence of Mechanical Shaft Subsystem

According to the above discussion, it is indicated that the relationship between electromagnetic torque perturbation $\hat{T}_e$ and rotor electrical angular position disturbance $\hat{\theta}_r$ serves as a bridge between the electrical and mechanical subsystems. This is because the electromagnetic torque acts on the rotor and interacts with the primary mechanical torque to drive the rotor's rotation. As is well known, greater rotor inertia means a stronger capability to maintain its operational status under small perturbations, suggesting that electrical harmonics are less likely to excite mechanical disturbances. In other words, the influence of electro-mechanical coupling on the impedance characteristic is reduced.

The Bode plots of the PMSG-WT equivalent positive-sequence impedance $Z^{\mathrm{p}}_{\mathrm{equ}}(s)$ with different rotor inertia time

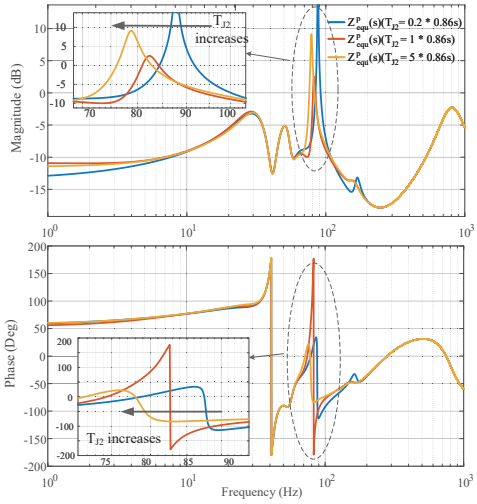

(a) Shaping effect of rotor inertia

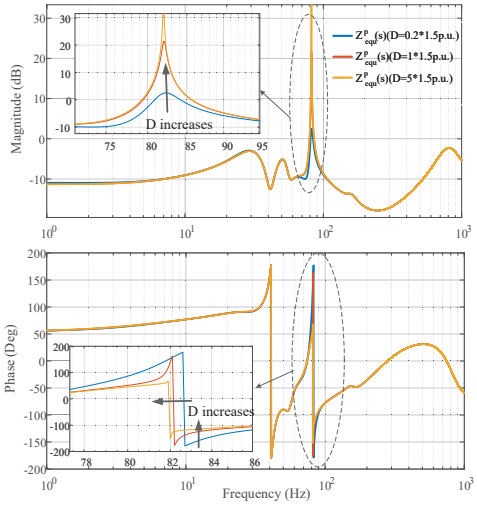

(b) Shaping effect of shaft damping

Fig. 8. Influence analysis of mechanical shaft subsystem

constants T_{J2} are illustrated to verify this discussion. The connected weak grid is the same as in Sec.2.4 with an SCR of 2. As shown in Fig.8(a), varying rotor inertia mainly affects the curves of $Z^{\mathrm{p}}_{\mathrm{equ}}(s)$ within the super-synchronous frequency band. As the value of T_{J2} increases, the resonant

Table 2
Control Parameters of PMSG-WT system.

Parameters	Descriptions	Values
K_{pp}/K_{pi}	PLL PI gain	0.3069/25.2437
K_{sp}/K_{si}	GSC current controller	0.0002/0.0463
K_{vp}/K_{vi}	GSC voltage controller	1.5838/195.0837
K_{wp}/K_{wi}	MSC speed controller	5/50
K_{rp}/K_{ri}	MSC current controller	0.0004/0.085

peak frequency of the impedance amplitude curve shifts to the left, and significant changes in phase occur near the resonant peak. When T_{J2} varies between 1/5 to 5 times its original value (0.86 s), the phase at the same frequency can vary by approximately 260 degrees. According to [22, 31], the weak-grid-tied PMSG system is at high risk of super-synchronous oscillation, but the substantial phase gap may lead to different stability analysis results depending on the varying rotor inertia, as reflected in this paper.

The damping coefficient D of the coupling shaft between the wind turbine and rotor is typically used to measure the relationship between damping torque and rotational speed change. A larger D indicates a greater damping effect of the shaft and a smaller change in rotational speed under the same torque perturbation. Therefore, the damping coefficient D also influences harmonic transfer between the mechanical and electrical subsystems. The effect of shaft damping is shown in Fig. 8(b) with different values of D. Similar to the effect of inertia, changes in D also affect the positive impedance $Z^{\mathrm{p}}_{\mathrm{equ}}(s)$ within the super-synchronous frequency band, primarily affecting the phase response. However, compared to the influence of T_{J2}, the effect of D is less pronounced. When D increases from 1/5 to 5 times its original value (1.5 p.u.), the resonant peak frequency slightly shifts to the left, and the phase gradually approaches 90° and −90°.

Therefore, both rotor inertia T_{J2} and damping coefficient D influence the strength of the coupling between the electrical and mechanical subsystems, primarily by affecting the harmonic transfer of electromagnetic torque $\hat{T}_{\mathrm{e}}$ to the angular position disturbance $\hat{\theta}_{\mathrm{r}}$. An increase in T_{J2} and D indicates greater damping in the mechanical system's response, which leads to a weaker electro-mechanical coupling effect. It is important to note that the trends resulting from changes in the shaft system parameters are influenced by the fundamental electrical parameters and control settings. However, these trends may not be entirely consistent across different wind turbine parameter settings.

4. Case Study

A weak-grid-tied PMSG-WT system is constructed in MATLAB/Simulink for case study, incorporating both the mechanical shaft subsystem and the electrical subsystem, as illustrated in Fig.1. The circuit parameters are as specified in TABLE1, and the control parameters are detailed in TABLE 2. Time-domain simulations are performed in this section to validate the effects of electro-mechanical coupling analyzed in the preceding sections.

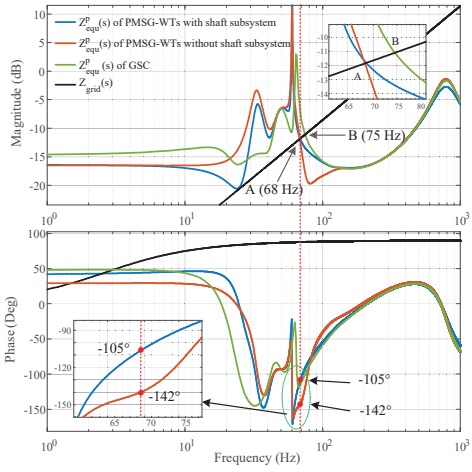

(a) Bode plot of system impedance

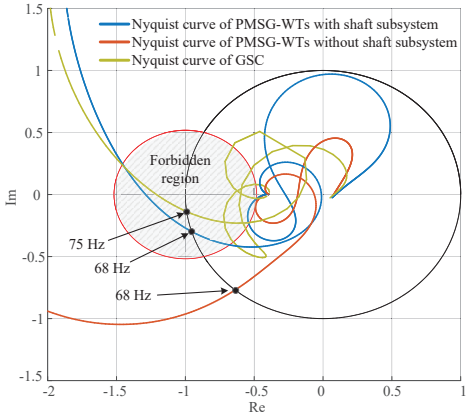

(b) Nyquist plot of system stability analysis

Fig. 9. Oscillation analysis of the weak-grid-tied PMSG-WTs system

As shown in Fig.9(a), the impedance bode plot of the grid-connected PMSG-WT system, which includes the mechanical shaft subsystem as described in (18), indicates that the system is at risk of instability with a phase margin of 15° at 68 Hz. This is because the PMSG-WT and the weak grid with an SCR of 2 form an equivalent RLC resonant circuit with insufficient phase margin. In contrast, Fig.9(a) also illustrates the impedance of a PMSG-WT without the mechanical shaft subsystem and a simplified GSC model with DC-bus dynamics. The PMSG-WT model without the shaft subsystem has a phase margin of 52° at 68 Hz, indicating a stable system. For the simplified GSC model, the impedance amplitude curve intersects with the grid impedance amplitude curve at 75 Hz, with a phase margin of 13°, which is insufficient for stability.

Furthermore, the Nyquist criterion is applied to analyze the stability of the interconnected system, as shown in Fig.9(b). To facilitate intuitive judgment, a forbidden region centered at $(-1, j0)$ with a radius of R_{min} is defined based on the maximum peak criterion (MPC) [32], as illustrated by the gray area. The forbidden radius R_{min} is determined based on the desired gain margin (GM) and phase margin

(PM), given by (20). In this study, the target values for GM and PM are chosen as 2 dB and 30°, respectively. If the impedance ratio curve enters the forbidden region, it indicates that the PM or GM is insufficient, and the system is at risk of oscillations.

$$R_{\min} = \max\left\{ 2\sin\left(\frac{PM}{2}\right), \quad 1 - \frac{1}{GM} \right\}. \tag{20}$$

For the PMSG-WT model that includes the shaft subsystem, the Nyquist curve enters the forbidden region, indicating insufficient stability margin and a risk of oscillation at 68 Hz. This frequency corresponds to the intersection point between the impedance loci and the unit circle. In contrast, when the mechanical shaft subsystem is not considered, the impedance ratio curve remains outside the forbidden region, suggesting a sufficient stability margin and indicating that the system can be considered stable. For the simplified GSC model, the Nyquist curve shows an unstable system with a risk of oscillation at 75 Hz.

Correspondingly, due to the frequency coupling effect observed in the Hami accident, both the impedance bode plot and Nyquist criterion predict potential current oscillation issues at 68/32 Hz for the PMSG-WT model that includes the shaft subsystem. This is contrary to the stability conclusions drawn from the PMSG-WT model without the shaft subsystem. Meanwhile, the impedance model of the GSC predicts instability with current oscillation issues at 75/25 Hz. Therefore, time-domain simulations are necessary to further validate the model effectiveness, as they better reflect the actual system dynamics.

In Fig.10, time-domain simulation experiments are conducted to validate the theoretical analysis discussed earlier. The grid impedance is changed from SCR=3 to SCR=2 at $t = 10$ s, while a small disturbance is injected at the PCC for stability verification. Before 10s, the system operates stably. However, upon injecting the disturbance, oscillations appear in the output current, voltage, and power waveforms at the PCC, as well as in the DC-bus voltage V_{dc}, as shown in Fig.10(a). The FFT results in Fig. 11 reveal that the current oscillates at 68 Hz and 32 Hz, which aligns with the analysis results using the PMSG-WT impedance model that includes the mechanical shaft subsystem. This confirms that neglecting the electro-mechanical coupling effect and omitting the machine-side models, including the MSC and generator, results in errors in the analytical model and can lead to inaccuracies in grid-connected stability analysis.

Furthermore, the drive-train torsional oscillation observed is a consequence of the electrical oscillation. The stator current harmonics generate electromagnetic torque disturbances through the magnetic flux of the generator, which in turn affects the rotatory speed at 18 Hz, as shown in Fig.10(b) and Fig.11. These simulation results align with the predictions from the bode plot in Fig. 9(a). As previously analyzed, disturbances in rotatory speed $\hat{\omega}_r$ lead to disturbances in angular displacement $\hat{\theta}_r$, which then affect the output current through the Park transform in the MSC controller.

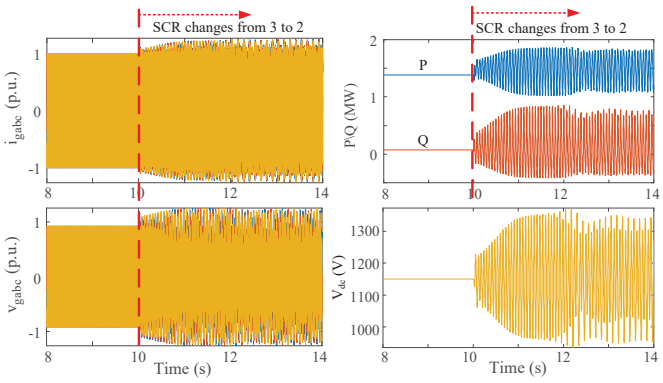

(a) Oscillation waveform at PCC

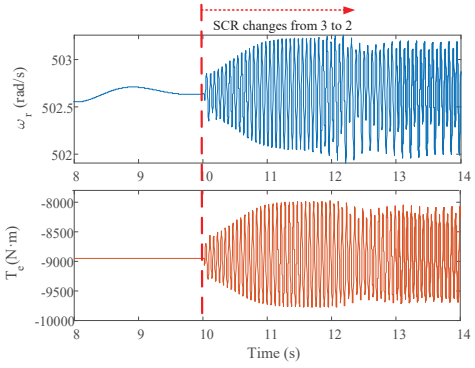

(b) Waveform of rotating speed and electromagnetic torque

Fig. 10. Oscillation results in time-domain of the weak-grid-tied PMSG system

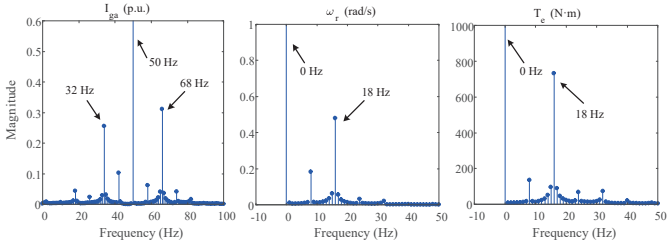

Fig. 11. Oscillation results in frequency-domain of the weak-grid-tied PMSG system

Therefore, the analysis and numerical simulation in this case validate that the electro-mechanical coupling effect between the electrical and mechanical subsystems in PMSG-WT systems significantly impacts grid-connected system stability.

5. Conclusion

This paper proposes an impedance model for PMSG-WTs that accounts for the electro-mechanical coupling effect, aiming to highlight the importance of including the mechanical subsystem in the study of electrical oscillation issues. The paper specifically describes the harmonic transfer relationship between the mechanical and electrical subsystems of PMSG-WTs, detailing the influence of the

electro-mechanical coupling effect on the output impedance characteristics. The following conclusions can be drawn:

- The electro-mechanical coupling effect can impact the entire output impedance of PMSG-WTs through the following process. The presence of harmonics in current and voltage in the WTs' electrical subsystem can cause electromagnetic torque disturbances $\hat{T}$e in the generator. This, in turn, can lead to disturbances in both the rotatory angular speed $\hat{\omega}$r and the electrical angular position $\hat{\theta}$r in the rotor shaft system. As a result, the transformation from abc to dq-frame during the modulation process in the MSC, which measures $\hat{\theta}$r, can affect the output stator current and voltage harmonics.
- The strength of electro-mechanical coupling effect can be affected by the rotor inertia T_{J2} and damping coefficient D in the shaft system, mainly through affecting the harmonic transfer of electromagnetic torque $\hat{T}_{\mathrm{e}}$ to the angular position disturbance $\hat{\theta}_{\mathrm{r}}$. Increasing T_{J2} and D means that there is more damping to the change of the mechanical system states, and also means weaker electro-mechanical coupling effect.
- The proposed impedance model of PMSG-WTs takes the electro-mechanical coupling effect into consideration, which can provide a more accurate stability analysis tool for electrical oscillations.

The results demonstrated that the mechanical subsystem has a significant influence on the electrical output characteristics. Considering the diversity of WT types, controllers, and parameters, future research will focus on measuring and evaluating the applicability range of different impedance models. This will help in selecting more practical analytical models while ensuring analysis accuracy.

A. Expressions of impedance model coefficient matrices

The coefficient matrix in the generator model is

$$\mathbf{G}_1 = \begin{bmatrix} e^{-j\varphi_0} & e^{j\varphi_0} \\ -je^{-j\varphi_0} & je^{j\varphi_0} \end{bmatrix},$$

$$\mathbf{G}_2 = \begin{bmatrix} \left(R_{\mathrm{s}} + s_1 L_{\mathrm{d}} + j\Omega_{\mathrm{r}} L_{\mathrm{q}}\right) e^{-j\varphi_0} & \left(R_{\mathrm{s}} + s_1 L_{\mathrm{d}} - j\Omega_{\mathrm{r}} L_{\mathrm{q}}\right) e^{j\varphi_0} \\ -j\left(R_{\mathrm{s}} + s_1 L_{\mathrm{q}} + j\Omega_{\mathrm{r}} L_{\mathrm{d}}\right) e^{-j\varphi_0} & j\left(R_{\mathrm{s}} + s_1 L_{\mathrm{q}} - j\Omega_{\mathrm{r}} L_{\mathrm{d}}\right) e^{j\varphi_0} \end{bmatrix},$$

$$\mathbf{G}_3 = \frac{1}{2}\begin{bmatrix} \left\{ \begin{array}{r} j(V_{\mathrm{s1}} e^{-j\varphi_0} - V_{\mathrm{s1}}^* e^{j\varphi_0}) - j(R_{\mathrm{s}} + s_1 L_{\mathrm{d}} + j\Omega_{\mathrm{r}} L_{\mathrm{q}}) I_{\mathrm{s1}} e^{-j\varphi_0} \\ +j(R_{\mathrm{s}} + s_1 L_{\mathrm{d}} - j\Omega_{\mathrm{r}} L_{\mathrm{q}}) I_{\mathrm{s1}}^* e^{j\varphi_0} - 2s_1 L_{\mathrm{q}} I_{\mathrm{qs}} \end{array} \right\} \\ \left\{ \begin{array}{r} (V_{\mathrm{s1}} e^{-j\varphi_0} + V_{\mathrm{s1}}^* e^{j\varphi_0}) - (R_{\mathrm{s}} + s_1 L_{\mathrm{q}} + j\Omega_{\mathrm{r}} L_{\mathrm{d}}) I_{\mathrm{s1}} e^{-j\varphi_0} \\ -(R_{\mathrm{s}} + s_1 L_{\mathrm{q}} - j\Omega_{\mathrm{r}} L_{\mathrm{d}}) I_{\mathrm{s1}}^* e^{j\varphi_0} - 2s_1 (L_{\mathrm{d}} I_{\mathrm{ds}} + \varphi_{\mathrm{m}}) \end{array} \right\} \end{bmatrix},$$

where, L_{d}, L_{q}, R_{s} represent the stator inductance along the dq-axis and stator resistance, respectively.

The coefficient matrices in the GSC model are

$$\mathbf{P}_1 = \frac{1}{2} K_{\mathrm{m}} \begin{bmatrix} V_{\mathrm{dc}}^{\mathrm{ref}} H_{\mathrm{si}}(s_1) H_{\mathrm{v}}(s_1) + M_{\mathrm{i1}} \\ V_{\mathrm{dc}}^{\mathrm{ref}} H_{\mathrm{si}}(s_1) H_{\mathrm{v}}(s_1) + M_{\mathrm{i1}}^* \end{bmatrix},$$

$$\mathbf{P}_2 = K_{\mathrm{m}} V_{\mathrm{dc}}^{\mathrm{ref}} \begin{bmatrix} -H_{\mathrm{si}}(s_1) + jK_{\mathrm{sd}} & 0 \\ 0 & -H_{\mathrm{si}}(s_1) - jK_{\mathrm{sd}} \end{bmatrix},$$

$$\mathbf{P}_3 = \frac{1}{2} K_{\mathrm{m}} V_{\mathrm{dc}}^{\mathrm{ref}} T_{\mathrm{PLL}}(s_1) \cdot \begin{bmatrix} (H_{\mathrm{si}}(s_1) - jK_{\mathrm{sd}}) I_{\mathrm{g1}} + M_{\mathrm{i1}} & -(H_{\mathrm{si}}(s_1) - jK_{\mathrm{sd}}) I_{\mathrm{g1}} - M_{\mathrm{i1}} \\ -(H_{\mathrm{si}}(s_1) + jK_{\mathrm{sd}}) I_{\mathrm{g1}}^* - M_{\mathrm{i1}}^* & (H_{\mathrm{si}}(s_1) + jK_{\mathrm{sd}}) I_{\mathrm{g1}}^* + M_{\mathrm{i1}}^* \end{bmatrix}.$$

The coefficient matrices in the MSC model are

$$\mathbf{Q}_1 = \frac{1}{2} K_{\mathrm{m}} \left[M_{\mathrm{r1}}, M_{\mathrm{r1}}^* \right]^T,$$

$$\mathbf{Q}_2 = K_{\mathrm{m}} V_{\mathrm{dc}}^{\mathrm{ref}} \begin{bmatrix} -H_{\mathrm{ri}}(s_1) & 0 \\ 0 & -H_{\mathrm{ri}}(s_1) \end{bmatrix},$$

$$\mathbf{Q}_3 = \frac{1}{2} K_{\mathrm{m}} V_{\mathrm{dc}}^{\mathrm{ref}} \begin{bmatrix} \left\{ \begin{array}{r} [jH_{\mathrm{ri}}(s_1) + K_{rd}] I_{\mathrm{s1}} + (j-1) e^{j\varphi_0} \\ +js_1 e^{j\varphi_0} H_{\omega}(s_1) H_{\mathrm{ri}}(s_1) \end{array} \right\} \\ \left\{ \begin{array}{r} [-jH_{\mathrm{ri}}(s_1) + K_{rd}] I_{\mathrm{s1}}^* - (j+1) e^{-j\varphi_0} \\ -js_1 e^{-j\varphi_0} H_{\omega}(s_1) H_{\mathrm{ri}}(s_1) \end{array} \right\} \end{bmatrix}.$$

The coefficient matrices in DC-bus model are

$$\begin{array}{l} \mathbf{E}_1 = \Lambda \begin{bmatrix} I_{\mathrm{g1}}^* & I_{\mathrm{g1}} \end{bmatrix}, \\ \mathbf{E}_2 = \Lambda \begin{bmatrix} V_{\mathrm{i1}}^* & V_{\mathrm{i1}} \end{bmatrix}, \\ \mathbf{E}_3 = \Lambda \begin{bmatrix} I_{\mathrm{s1}}^* & I_{\mathrm{s1}} \end{bmatrix}, \\ \mathbf{E}_4 = \Lambda \begin{bmatrix} V_{\mathrm{s1}}^* & V_{\mathrm{s1}} \end{bmatrix}, \end{array}$$

where

$$\Lambda = -3/\left(2s_1 V_{\mathrm{dc}}^{\mathrm{ref}} C_{\mathrm{dc}}\right), s_1 = j2\pi(f_{\mathrm{p}} - f_1).$$

The coefficient matrices in electromagnetic torque are

$$\mathbf{T} = \begin{bmatrix} T_1(s_1) & T_2(s_1) \end{bmatrix},$$

where

$$T_1(s_1) = \frac{-j6p^2\left[(L_{\mathrm{d}} - L_{\mathrm{q}}) I_{\mathrm{s1}} + \psi_{\mathrm{m}}\right] e^{-j\varphi_0}}{4M(s_1) + 3p^2\left[(L_{\mathrm{d}} - L_{\mathrm{q}})(I_{\mathrm{s1}}^2 e^{-j\varphi_0} + I_{\mathrm{s1}}^{*\,2} e^{j\varphi_0}) + \psi_{\mathrm{m}}(I_{\mathrm{s1}} e^{-j\varphi_0} + I_{\mathrm{s1}}^* e^{j\varphi_0})\right]},$$

$$T_2(s_1) = \frac{j6p^2\left[(L_{\mathrm{d}} - L_{\mathrm{q}}) I_{\mathrm{s1}}^* + \psi_{\mathrm{m}}\right] e^{j\varphi_0}}{4M(s_1) + 3p^2\left[(L_{\mathrm{d}} - L_{\mathrm{q}})(I_{\mathrm{s1}}^2 e^{-j\varphi_0} + I_{\mathrm{s1}}^{*\,2} e^{j\varphi_0}) + \psi_{\mathrm{m}}(I_{\mathrm{s1}} e^{-j\varphi_0} + I_{\mathrm{s1}}^* e^{j\varphi_0})\right]}.$$

References

[1] J. Hu, Q. Hu, B. Wang, H. Tang, Y. Chi, Small signal instability of PLL-synchronized type-4 wind turbines connected to high-impedance ac grid during LVRT, IEEE Trans. Energy Conver. 31 (4) (2016) 1676–1687.

[2] B. Liu, Z. Li, X. Zhang, X. Dong, X. Liu, Impedance-based analysis of control interactions in weak-grid-tied PMSG wind turbines, IEEE J. Emerg. Sel. Topics Circuits Syst.

[3] D. Xie, Y. Lu, J. Sun, C. Gu, Small signal stability analysis for different types of pmsgs connected to the grid, Renewable Energy 106 (2017) 149–164.

[4] S. Li, Low-frequency oscillations of wind power systems caused by doubly-fed induction generators, Renewable Energy 104 (2017) 129–138.

[5] F. Arraño-Vargas, S. Jiang, B. Bennett, G. Konstantinou, Mitigation of power system oscillations in weak grids with battery energy storage systems: A real-world case study, Energy 283 (2023) 128648.

[6] Y. Cheng, L. Fan, J. Rose, S.-H. Huang, J. Schmall, X. Wang, X. Xie, J. Shair, J. R. Ramamurthy, N. Modi, C. Li, C. Wang, S. Shah, B. Pal, Z. Miao, A. Isaacs, J. Mahseredjian, J. Zhou, Real-world subsynchronous oscillation events in power grids with high penetrations of inverter-based resources, IEEE Trans. Power Syst. 38 (1) (2022) 316–330.

[7] L. Fan, Z. Miao, S. Shah, Y. Cheng, J. Rose, S.-H. Huang, B. Pal, X. Xie, N. Modi, S. Wang, S. Zhu, Real-world 20-hz ibr subsynchronous oscillations: Signatures and mechanism analysis, IEEE Trans. Energy Conver. 37 (4) (2022) 2863–2873.

[8] W. Wang, G. Li, J. Guo, Large-scale renewable energy transmission by hvdc: Challenges and proposals, ENGINEERING-PRC 19 (2022) 252–267.

[9] H. Geng, D. Xu, Stability analysis and improvements for variable-speed multipole permanent magnet synchronous generator-based wind energy conversion system, IEEE Trans. Sustain. Energ. 2 (4) (2011) 459–467.

[10] C. Zhu, Y. Qiu, T. Wang, Dynamic stall of the wind turbine airfoil and blade undergoing pitch oscillations: A comparative study, Energy 222 (2021) 120004.

[11] J. Ma, L. Wang, Y. Shen, A. Phadke, Interaction energy-based stability analysis method and application in grid-tied type-4 wind turbine generator, IEEE J. Emerg. Sel. Topics Power Electr. 9 (5) (2020) 5542–5557.

[12] L. Chen, X. Du, B. Hu, F. Blaabjerg, Drivetrain oscillation analysis of grid forming type-IV wind turbine, IEEE Trans. Energy Conver. 37 (4) (2022) 2321–2337.

[13] F. Fateh, W. N. White, D. Gruenbacher, Torsional vibrations mitigation in the drivetrain of DFIG-based grid-connected wind turbine, IEEE Trans. Ind. Applicat. 53 (6) (2017) 5760–5767.

[14] H. Liu, X. Xie, W. Liu, An oscillatory stability criterion based on the unified dq-frame impedance network model for power systems with high-penetration renewables, IEEE Trans. Power Syst. 33 (3) (2018) 3472–3485.

[15] M. Zhang, X. Yuan, J. Hu, Mechanism analysis of subsynchronous torsional interaction with PMSG-based wts and LCC-HVDC, IEEE J. Emerg. Sel. Topics Power Electr. 9 (2) (2021) 1708–1724.

[16] Y. Xu, M. Zhang, L. Fan, Z. Miao, Small-signal stability analysis of type-4 wind in series-compensated networks, IEEE Trans. Energy Conver. 35 (1) (2020) 529–538.

[17] L. Fan, Z. Miao, L. Bao, S. Shah, R. H. Ramakrishna, DQ admittance model extraction for IBRs via gaussian pulse excitation, IEEE Trans. Power Syst.

[18] B. Wen, B. Dushan, B. Rolando, M. Paolo, Z. Shen, Analysis of dq small-signal impedance of grid-tied inverters, IEEE Trans. Power Electr. 31 (1) (2015) 675–687.

[19] A. Nair, S. Kamalasadan, J. Geis-Schroer, S. Patel, M. Smith, An investigation of grid stability and a new design of adaptive phase-locked loop for wind-integrated weak power grid, IEEE Trans. Ind. Applicat. 58 (5) (2022) 5871–5884.

[20] Y. Li, L. Fan, Z. Miao, Wind in weak grids: Low-frequency oscillations, subsynchronous oscillations, and torsional interactions, IEEE Trans. Power Syst. 35 (1) (2020) 109–118.

[21] Y. Xu, H. Nian, L. Chen, Small-signal modeling and analysis of DC-link dynamics in type-IV wind turbine system, IEEE Trans. Ind. Electron. 68 (2) (2020) 1423–1433.

[22] B. Liu, Z. Li, X. Dong, S. S. Yu, X. Chen, A. M. Oo, X. Lian, Z. Shan, X. Liu, Impedance modeling and controllers shaping effect analysis of pmsg wind turbines, IEEE J. Emerg. Sel. Topics Power Electr. 9 (2) (2020) 1465–1478.

[23] C. Zhang, X. Cai, M. Molinas, A. Rygg, On the impedance modeling and equivalence of ac/dc-side stability analysis of a grid-tied type-iv wind turbine system, IEEE Trans. Energy Conver. 34 (2) (2019) 1000–1009.

[24] A. Khodamoradi, P. Mattavelli, F. Cavazzana, Effect of torsional interactions on the output impedance of PMSG-based wind turbines, in: European Conference on Power Electronics and Applications, 2018, pp. P–1.

[25] A. Avazov, F. Colas, J. Beerten, X. Guillaud, Damping of torsional vibrations in a type-IV wind turbine interfaced to a grid-forming converter, in: IEEE Madrid PowerTech, 2021, pp. 1–6.

[26] M. Céspedes, J. Sun, Impedance modeling and analysis of grid-connected voltage-source converters, IEEE Trans. Power Electr. 29 (3) (2014) 1254–1261.

[27] Y. Xu, H. Nian, J. Sun, Cross coupling of grid-connected inverter impedance over frequency - phenomena, effects and modeling, in: Proc. Wind Integration Workshop., Vienna, Austria, 2016, pp. 1–8.

[28] I. Vieto, J. Sun, Sequence impedance modeling and converter-grid resonance analysis considering DC bus dynamics and mirrored harmonics, in: Proc. IEEE W. Contr. Model. Power Electr., Padova, Italy, 2018, pp. 1–8.

[29] H. Wang, C. Buchhagen, M. Greve, J. Sun, Methods to aggregate turbine and network impedance for wind farm resonance analysis, in: Proc. Wind Integration Workshop., Stockholm, Sweden, 2018, pp. 1–6.

[30] I. Vieto, J. Sun, Refined small-signal sequence impedance models of type-III wind turbines, in: Proc. IEEE Ener. Conv., Portland, OR, USA, 2018, pp. 2242–2249.

[31] H. Liu, X. Xie, J. He, T. Xu, Z. Yu, C. Wang, C. Zhang, Subsynchronous interaction between direct-drive PMSG based wind farms and weak AC networks, IEEE Trans. Power Syst. 32 (6) (2017) 4708–4720.

[32] S. Vesti, T. Suntio, J. A. Oliver, R. Prieto, J. A. Cobos, Impedance-based stability and transient-performance assessment applying maximum peak criteria, IEEE Trans. Power Electr. 28 (5) (2013) 2099–2104.